Complex Wave and Phase Retrieval from A Single Off-Axis Interferogram

GANG LUO[1], YANPING HE[2], XIN SHU[2], RENJIE ZHOU[2], AND THIERRY BLU[1,*]

[1] Department of Electronic Engineering, The Chinese University of Hong Kong, Shatin, N.T., Hong Kong, China
[2] Department of Biomedical Engineering, The Chinese University of Hong Kong, Shatin, N.T., Hong Kong, China
[*] Corresponding author: thierry.blu@m4x.org

Compiled November 30, 2022

Single-frame off-axis holographic reconstruction is promising for quantitative phase imaging. However, reconstruction accuracy and contrast are degraded by noise, frequency spectrum overlap of the interferogram, severe phase distortion, etc. In this work, we propose an iterative single-frame complex wave retrieval that is based on an explicit model of the object and reference waves. We also develop a novel phase restoration algorithm which does not resort to phase unwrapping. Both simulation and real experiments demonstrate higher accuracy and robustness compared to the state-of-the-art methods, both for the complex wave estimation, and the phase reconstruction. Importantly, the allowed bandwidth for the object wave is significantly improved in realistic experimental conditions (similar amplitude for the object and reference waves), which makes it attractive for large field-of-view and high-resolution imaging applications.

http://dx.doi.org/10.1364/ao.XX.XXXXXX

1. INTRODUCTION

Holography, pioneered by Dennis Gabor [1], is a well-established interferometric technique whereby a complex-valued object wave, especially its phase, is reconstructed from the image of its interferences with a reference beam [2, 3], named interferogram. Benefiting from being label-free, non-invasive, and fast, it has found a wide range of applications in metrology [4], Fourier ptychographic microscopy [5], quantitative phase microscopy [6, 7], optical diffraction tomography [8], etc. Despite the development of increasingly sophisticated reconstruction algorithms, noise degradation and restrictive reconstruction hypotheses (e.g., bandwidth limitations) are obstacles to high-resolution phase estimation. For instance, an extra interferogram from an object-free region usually needs to be acquired for calibration purpose [9, 10]. As cells tend to assemble in close proximity during growth, it is often difficult to capture adequate calibration images. This outlines the advantage of single-frame acquisitions which, additionally, increase the image throughput significantly, without apparent loss of quality [11, 12]. Limitations on the frequency overlap of the main constituents of an interferogram, uncontrolled phase distortion, etc. also restrict the development of multiplex, high-resolution and large filed-of-view (FOV) off-axis based quantitative phase imaging [12, 13].

In this paper, we address the reconstruction of an off-axis digital hologram (DH) from a single-frame acquisition. The most standard reconstruction method, the Fourier filtering approach [14, 15], is the benchmark of linear methods. It discards the information contained in the 0^{th} order and in the mirror object frequency bands of an interferogram (i.e., the -1^{st} order), by applying a windowed filter. Hence, a good separation of the frequency bands involved is required, so as to ensure a reconstruction of good quality, in particular of the phase of the object complex wave [15]. In contrast, non-linear methods do not suppress the information contained in the 0^{th} and $\pm 1^{\text{st}}$ order bands; instead, they are able to exploit it, even in situations where frequency bands overlap. This is exemplified in temporal phase-shifting methods [16, 17], which require three or more interferograms to be captured sequentially and a precise control of the spatial frequency of the reference wave. Nowadays, with the advances of coded devices, a couple of interference patterns can be encoded in only a single acquisition [13, 18], albeit with some resolution loss. This is an example of local image reconstruction (pixels are retrieved from the same neighborhood in the interferograms), as opposed to global image reconstruction (often based on frequency band assumptions). Other non-linear methods are summarized below:

- Liebling's method [19]: local, resolution inversely related to window size (used to reduce noise);
- Seelamantula's log method [20, 21]: global, quadrant support assumption for object wave;
- Kim's method [22]: local, exploits a similar idea as Liebling's method (constancy of the object wave in a small neighborhood), loss of resolution;

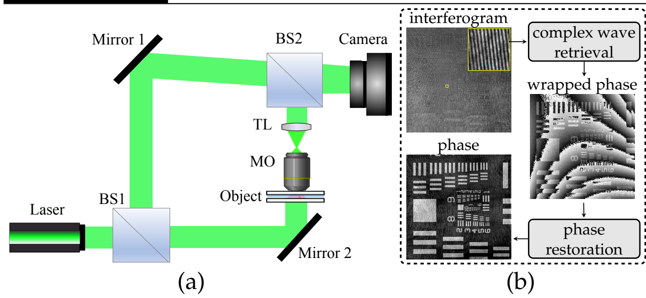

Fig. 1. (a) Schematic of a transparent off-axis geometry DH and (b) flowchart of the phase retrieval process. BS1&BS2: beam splitters; MO: microscope objective; TL: tube lens.

- Baek's Kramers–Kronig method [23]: global, object wave with (possibly large) circular frequency support.
- Total variation-based compressive sensing (CS) [24]: global, discards zeroth order (high-pass pre-filtering), ideal for piecewise-constant images.

Baek's method is basically a more robust version of Seelamantula's log method, thanks to different filtering options (in particular extra low-pass filtering). CS has been applied to in-line [25, 26] and off-axis [24, 27, 28] holographic reconstruction. Its quality of reconstruction highly depends on the regularization parameter which balances the data fidelity and regularization. And apart from Liebling's approach, an extra acquisition of the intensity of the reference wave is needed in order to retrieve the object wave. In addition, most of them assume that the reference wave has a larger intensity than the object wave. Rotation-covariant operators like the Hilbert spiral or the Riesz transforms can be also used to recover the phase of the complex wave (phase demodulation) [29–33], but these approaches require that the zeroth order of the hologram be removed completely (e.g., by filtering) which, again, may be difficult to achieve if the intensity of the object wave is not small compared to the reference wave.

Also to be more complete, we should mention iterative methods such as Fienup's [34] and Gerchberg-Saxton's [35] methods which are designed to retrieve the phase of complex-valued images from in-line intensity measurements (reference and object waves are on the same axis) or equivalent Fourier magnitude [36, 37] , but we will not consider them in this paper because they have not been used in off-axis context. As a sign of the times, Deep learning approaches have also been used for holographic reconstruction [38–40], but they inevitably require large training data, and may eventually be less reliable in diverse experimental configurations of camera and light source.

Once the complex object wave has been reconstructed, performing quantitative phase analysis requires phase restoration as well. This is particularly so in applications like high-resolution phase imaging of cells where magnification factors are high. This is a challenge for single-frame methods because they cannot easily separate the intrinsic distortion of the reference wave and other optical distortions. High-order phase distortions (such as tilt, coma, astigmatism, spherical aberration) appear naturally [41, 42] in optical systems with high numerical aperture (NA) and transverse magnification. Compensation by only adjusting the lens is likely to be insufficient, thus calling for a more computational approach. Conventionally, phase restoration involves not only phase unwrapping but also numerical fitting procedures [42, 43]. Artifacts can easily be induced in the phase unwrapping process, as a consequence of fast phase variations, noise, and other singularities, mentioned in [44]. Current approaches based on optimized phase unwrapping [45] and aberration compensation [46] usually have a significant computational cost.

In order to address the various issues that we have identified so far, we propose a complete solution for single-frame phase estimation, made of a complex wave retrieval algorithm and a phase restoration algorithm.

First, we devise a linear model to represent the reference and object waves, thereby over-determining the original under-determined complex wave retrieval problem—hence, bypassing the need to regularize. Based on this model, we minimize an interferogram-fitting criterion which enjoys an efficient iterative implementation. We also give an idea of the convergence behaviour of this algorithm for a wide variety of the main parameters, notably when the frequency band of the object wave has a large overlap with the other frequency orders present in the interferogram, and when the reference wave has a smaller amplitude than the object wave. We even show that it is possible to reconstruct accurately the object wave when its frequency band occupies half of the sampling band of the interferogram, i.e., the maximum theoretically possible. These results suggest that our method is able to achieve high-resolution, large FOV, and multiplexing in quantitative phase imaging.

Second, we develop a fast, highly accurate and robust phase restoration algorithm that is able to fit accurately a wrapped phase image, without using any unwrapping intermediates.

2. METHOD

A. Complex Wave Retrieval Algorithm

The interference between an object wave $U_\mathrm{O}(\mathbf{r})$ and a reference wave $U_\mathrm{R}(\mathbf{r})$ at the camera plane is the general setting that results in an interferogram $I(\mathbf{r})$ in traditional DH microscopy:

$$\begin{aligned} I(\mathbf{r}) &= \left|U_\mathrm{O}(\mathbf{r}) + U_\mathrm{R}(\mathbf{r})\right|^2 \\ &= \underbrace{|U_\mathrm{O}(\mathbf{r})|^2 + |U_\mathrm{R}(\mathbf{r})|^2}_{0^{\text{th}}\ \text{Order}} + \underbrace{U_\mathrm{O}^*(\mathbf{r})U_\mathrm{R}(\mathbf{r})}_{-1^{\text{st}}\ \text{Order}} + \underbrace{U_\mathrm{O}(\mathbf{r})U_\mathrm{R}^*(\mathbf{r})}_{+1^{\text{st}}\ \text{Order}} \end{aligned} \quad \textbf{(1)}$$

where $\mathbf{r} = (x, y)$ is a two-dimensional vector which may take values over a range $\mathcal{D}$ (i.e., the extent of the camera CCD). The reference wave is typically of the form $U_\mathrm{R}(\mathbf{r}) = A_\mathrm{R}(\mathbf{r})\mathrm{e}^{j\mathbf{k}^\mathrm{T}\mathbf{r}}$ where $A_\mathrm{R}(\mathbf{r}) \in \mathbb{C}$ and $\mathbf{k} \in \mathbb{R}^2$ are its spatially-varying amplitude and spatial frequency, respectively. The slight tilt angle between reference and object waves ensures the frequency separation of these orders (see Fig. 1).

The main idea of the algorithm is based on the observation that, if the phase $\phi(\mathbf{r})$ of $U_\mathrm{O}(\mathbf{r}) + U_\mathrm{R}(\mathbf{r})$ is known, the problem is essentially a linear problem: extract $U_\mathrm{O}(\mathbf{r})$ and $U_\mathrm{R}(\mathbf{r})$ from $I(\mathbf{r})\mathrm{e}^{i\phi(\mathbf{r})}$, which can be achieved by assuming that $U_\mathrm{O}(\mathbf{r})$ and $U_\mathrm{R}(\mathbf{r})$ do not share the same spatial frequency band. Hence, a key ingredient is the estimation of $\phi(\mathbf{r})$.

Optimization Criterion We focus on the minimization of the (non-convex) criterion

$$\mathcal{F}\{U_\mathrm{O}, A_\mathrm{R}\} = \sum_{\mathbf{r}\in\mathcal{D}} \left(\sqrt{I(\mathbf{r})} - \left|U_\mathrm{O}(\mathbf{r}) + A_\mathrm{R}(\mathbf{r})\mathrm{e}^{j\mathbf{k}^\mathrm{T}\mathbf{r}}\right|\right)^2, \quad \textbf{(2)}$$

over $U_\mathrm{O}(\mathbf{r})$ and $A_\mathrm{R}(\mathbf{r})$, under the constraints (visualization in Fig. 2):

- $U_\mathrm{O}(\mathbf{r})$ is band-limited in some domain $\mathcal{B}_\mathrm{O}$ (lowpass, large support);
- $A_\mathrm{R}(\mathbf{r})$ is band-limited in some domain $\mathcal{B}_\mathrm{R}$ (lowpass, small support);

- The frequency supports of $U_{\mathrm{O}}(\mathbf{r})$ and $A_{\mathrm{R}}(\mathbf{r})\mathrm{e}^{j\mathbf{k}^{\mathrm{T}}\mathbf{r}}$ do not overlap; i.e., $\mathcal{B}_{\mathrm{O}} \cap \{\mathbf{k} + \mathcal{B}_{\mathrm{R}}\} = \emptyset$.

Note that by choosing the size of these frequency domains small enough, we transform the under-determined reconstruction problem into an over-determined one. And in practical implementation (digital hologram, discrete frequencies), it is more "natural" to assume that $U_{\mathrm{O}}(\mathbf{r})\mathrm{e}^{-j\mathbf{k}^{\mathrm{T}}\mathbf{r}}$ is band-limited in $\{-\mathbf{k} + \mathcal{B}_{\mathrm{O}}\}$, than to assume that $U_{\mathrm{O}}(\mathbf{r})$ is band-limited in $\mathcal{B}_{\mathrm{O}}$.

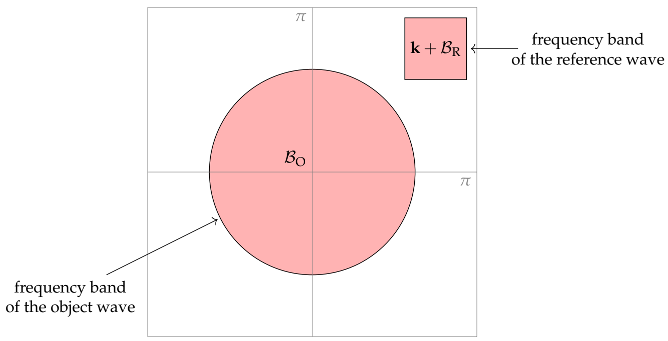

Fig. 2. Depiction of the frequency bands of the object wave ($\mathcal{B}_{\mathrm{O}}$) and the reference wave ($\mathcal{B}_{\mathrm{R}}$): $\mathcal{B}_{\mathrm{R}}$, shown larger than reality here, is typically discretized as a 3×3 block of DFT coefficients.The vector $\mathbf{k}$ denotes the central frequency of the reference wave $A_{\mathrm{R}}(\mathbf{r})\mathrm{e}^{j\mathbf{k}^{\mathrm{T}}\mathbf{r}}$.

The wave vector $\mathbf{k}$ can be estimated in the Fourier domain of the interferogram by locating the maximum of +1st order, for instance. The assumption that $U_{\mathrm{O}}(\mathbf{r})$ is low-pass is supported by the fact that, due to the limited aperture $\mathrm{NA} = n_i \sin\theta$ of a microscope objective, the spectrum of the object wave is typically limited by a cutoff frequency $2\pi\mathrm{NA}/\lambda$, where n_i, θ and λ are the refractive index of the surrounding medium, the maximal half-angle of light that enters or exits the objective, and the wavelength of the light in the free space, respectively [23, 47].

MM Optimization Algorithm To find a solution of this optimization problem, we build an iterative algorithm using a Majorization-Minimization (MM) approach [48] (see application to in-line holography [37, 49]): at iteration m, the optimization criterion $\mathcal{F}\{U_{\mathrm{O}}, A_{\mathrm{R}}\}$ is "majorized" (i.e., upper-bounded) by a simpler criterion (i.e., that can be minimized easily) $\mathcal{F}^{(m)}\{U_{\mathrm{O}}, A_{\mathrm{R}}\}$, and which also satisfies $\mathcal{F}\{U_{\mathrm{O}}^{(m)}, A_{\mathrm{R}}^{(m)}\} = \mathcal{F}^{(m)}\{U_{\mathrm{O}}^{(m)}, A_{\mathrm{R}}^{(m)}\}$. Then, the minimization of $\mathcal{F}^{(m)}\{U_{\mathrm{O}}, A_{\mathrm{R}}\}$ over $U_{\mathrm{O}}(\mathbf{r})$ and $A_{\mathrm{R}}(\mathbf{r})$, under the band-limitation constraint on U_{O}, provides the updated values $U_{\mathrm{O}}^{(m+1)}(\mathbf{r})$ and $A_{\mathrm{R}}^{(m+1)}(\mathbf{r})$: see Fig. 3 for an illustration.

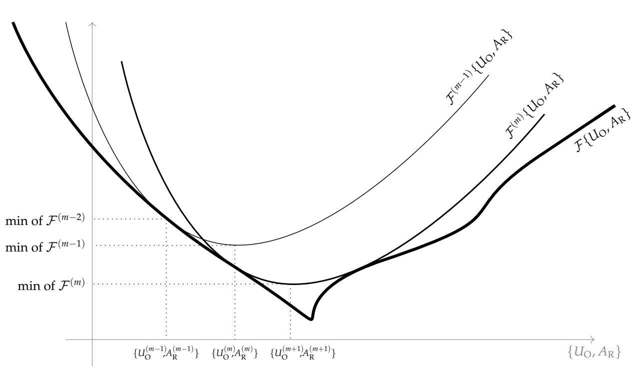

Fig. 3. Visual depiction of the Majorization-Minimization (MM) strategy for minimizing the functional $\mathcal{F}$.

Compared to a gradient descent approach, the MM strategy similarly guarantees that the criterion decreases at each iteration, but without the need for adjusting a step size. Moreover, non-smooth criteria like Eq. (2) can be used. Like gradient descent, an MM algorithm usually converges to a local optimum (with general assumptions [48]), but this solution is quite good in practice (we do not attempt to prove that it is the global minimum of our functional $\mathcal{F}$, though). We use the majorizer

$$\mathcal{F}^{(m)}\{U_{\mathrm{O}}, A_{\mathrm{R}}\} = \sum_{\mathbf{r}\in\mathcal{D}} \left| \sqrt{I(\mathbf{r})}\, \mathrm{e}^{j\phi^{(m)}(\mathbf{r})} - \left(U_{\mathrm{O}}(\mathbf{r}) + A_{\mathrm{R}}(\mathbf{r})\mathrm{e}^{j\mathbf{k}^{\mathrm{T}}\mathbf{r}}\right) \right|^2, \quad \textbf{(3)}$$

where $\phi^{(m)}(\mathbf{r}) = \arg\{U_{\mathrm{O}}^{(m)}(\mathbf{r}) + A_{\mathrm{R}}^{(m)}(\mathbf{r})\mathrm{e}^{j\mathbf{k}^{\mathrm{T}}\mathbf{r}}\}$, and which obviously satisfies the MM requirements

$$\mathcal{F}\{U_{\mathrm{O}}, A_{\mathrm{R}}\} \leq \mathcal{F}^{(m)}\{U_{\mathrm{O}}, A_{\mathrm{R}}\},$$
$$\mathcal{F}\{U_{\mathrm{O}}^{(m)}, A_{\mathrm{R}}^{(m)}\} = \mathcal{F}^{(m)}\{U_{\mathrm{O}}^{(m)}, A_{\mathrm{R}}^{(m)}\},$$

thanks to the triangular inequality ($\big||a| - |b|\big| \leq |a - b|$), and to the definition of $\phi^{(m)}$. Given that the majorizing criterion Eq. (3) is quadratic in function of $U_{\mathrm{O}}(\mathbf{r})$ and $A_{\mathrm{R}}(\mathbf{r})$, its minimization results in the orthogonal projection of $\sqrt{I(\mathbf{r})}\,\mathrm{e}^{j\phi^{(m)}(\mathbf{r})}$ onto the space of functions of frequency support limited to $\mathcal{B}_{\mathrm{O}}$ (for U_{O}) and $\mathcal{B}_{\mathrm{R}}$ (for A_{R}), equivalent to filtering in the frequency band considered—-"band-limitation". More specifically, the phase $\phi^{(m)}(\mathbf{r})$ is updated following the steps of Algorithm 1 (visualization in Fig. 6).

Algorithm 1. Complex Wave Retrieval Algorithm

Input: Interferogram $I(\mathbf{r})$
Output: Object wave $U_{\mathrm{O}}(\mathbf{r})$, reference wave $A_{\mathrm{R}}(\mathbf{r})\mathrm{e}^{j\mathbf{k}^{\mathrm{T}}\mathbf{r}}$

1: initialize the total phase $\phi^{(0)}(\mathbf{r})$.
2: **for** $m = 1$ to M **do**[a]
3: *band-limitation of* U_{R}: compute $A_{\mathrm{R}}^{(m+1)}(\mathbf{r})$ by filtering $\sqrt{I(\mathbf{r})}\,\mathrm{e}^{j\phi^{(m)}(\mathbf{r})}$ in the band $\{\mathbf{k} + \mathcal{B}_{\mathrm{R}}\}$;
4: *band-limitation of* U_{O}: compute $U_{\mathrm{O}}^{(m+1)}(\mathbf{r})$ by filtering $\sqrt{I(\mathbf{r})}\,\mathrm{e}^{j\phi^{(m)}(\mathbf{r})}$ in the band $\mathcal{B}_{\mathrm{O}}$;
5: *total phase update*: compute the total phase $\phi^{(m+1)}(\mathbf{r})$ from the argument of $U_{\mathrm{O}}^{(m+1)}(\mathbf{r}) + A_{\mathrm{R}}^{(m+1)}\mathrm{e}^{j\mathbf{k}^{\mathrm{T}}\mathbf{r}}$.
6: **end for**

[a] M is typically equal to 10.

The iterations can be stopped either when the reconstructed interferogram

$$I^{(m)}(\mathbf{r}) = \left|U_{\mathrm{O}}^{(m)}(\mathbf{r}) + A_{\mathrm{R}}^{(m)}(\mathbf{r})\mathrm{e}^{j\mathbf{k}^{\mathrm{T}}\mathbf{r}}\right|^2$$

is close enough to the true interferogram $I(\mathbf{r})$, or when changes to $I^{(m)}(\mathbf{r})$ are negligible, or simply after a fixed number of iterations. The evaluation metrics that we use to compare two images $I_1(\mathbf{r})$ and $I_2(\mathbf{r})$ (typically, the ground-truth complex wave, and its reconstruction by our algorithm), is the Peak Signal-to-Noise Ratio (PSNR), which is defined according to

$$\mathrm{PSNR}(I_1, I_2) = 10\log_{10}\left(\frac{N \max_{\mathbf{r}} |I_1(\mathbf{r})|^2}{\sum_{\mathbf{r}} |I_1(\mathbf{r}) - I_2(\mathbf{r})|^2}\right) \quad \mathrm{dB}, \quad \textbf{(4)}$$

where N denotes the number of pixels of these images. The advantages of this approach are:

1. Overlap of 0^{th} and $\pm 1^{\text{st}}$ orders is possible, in contrast with the traditional Fourier method.
2. Single-frame acquisition: in contrast to other state-of-the-art methods, no extra acquisition of an object-free interferogram or of the reference wave is needed.

3. Resolution is potentially as large as about $1/\sqrt{2}$ the resolution of the interferogram, significantly higher than any other methods.
4. Automatic adaptation to a spatially-varying reference wave.

We now give more details regarding these points in the subsection below.

Discussion

Computational Efficiency The typical computational cost of one iteration is mostly due to the three 2D FFT that are required in the calculation. This cost is roughly proportional to $N \ln N$, which means that, with a fixed number of iterations, the algorithm scales roughly like the number of pixels, at least for images of size 128×128 up to 1024×1024. Empirically, the whole optimization procedure does not require more than about 10 iterations—about 0.2 seconds on a standard laptop computer for a 512×512 image—before providing a good practical approximation of the solution; i.e., PSNR ≥ 25 dB (see below the paragraph "Key Parameters" and simulations in Fig. 5).

Phase Indeterminacy Obviously, if $U_\mathrm{O}(\mathbf{r})$ and $U_\mathrm{R}(\mathbf{r})$ minimize Eq. (2) under our band-limitation constraints, then $U_\mathrm{O}(\mathbf{r})\mathrm{e}^{i\theta}$ and $U_\mathrm{R}(\mathbf{r})\mathrm{e}^{i\theta}$ are also solutions, for an arbitrary constant phase $\theta \in (-\pi, \pi]$. This phase indeterminacy still holds approximately (i.e., numerically) for a slowly varying phase $\theta(\mathbf{r})$ because $U_\mathrm{O}(\mathbf{r})\mathrm{e}^{i\theta(\mathbf{r})}$ and $U_\mathrm{R}(\mathbf{r})\mathrm{e}^{i\theta(\mathbf{r})}$ have roughly the same bandwidth as $U_\mathrm{O}(\mathbf{r})$ and $U_\mathrm{R}(\mathbf{r})$: the "effective" bandwidth of $\mathrm{e}^{i\theta(\mathbf{r})}$ is small.

For this reason, the slowly varying phase of $A_\mathrm{R}(\mathbf{r})$ cannot be retrieved accurately within the scope of this algorithm. To mitigate this issue, we reduce the number of degrees of freedom used to describe $A_\mathrm{R}(\mathbf{r})$ by assuming that $A_\mathrm{R}(\mathbf{r})$ is real-valued, an extra linear constraint which amounts to taking the real part of the result of step (3). The slow phase variation of $A_\mathrm{R}(\mathbf{r})$ can later be estimated directly on the retrieved $U_\mathrm{O}(\mathbf{r})$ by using the phase restoration algorithm of Subsection B.

Key Parameters Since the criterion Eq. (2) is likely to have (many) local minima, the MM optimization approach that we proposed may only converge towards a suboptimal solution, depending how close our initialization is to the global minimum. Intuitively, it is the bandwidth $\mathcal{B}_\mathrm{O}$ of the object, the frequency $\mathbf{k}$ of the reference wave, and the amplitude of object wave relative to the reference wave that are the most influential. More specifically, we focus on the following simplified parameters

- Object/Reference amplitude ratio:

$$\mathrm{O/R} = \frac{\sum_\mathbf{r} |U_\mathrm{O}(\mathbf{r})|}{\sum_\mathbf{r} |U_\mathrm{R}(\mathbf{r})|}. \quad \textbf{(5)}$$

  This parameter is often assumed to be small in advanced complex wave reconstruction algorithms, conflicting with experimental settings where a value close to 1 is known to provide maximal SNR and fringe contrast [50, 51]. We do not have such an assumption here.
- Modulus of the frequency of the reference wave: $d = \|\mathbf{k}\| = \sqrt{k_x^2 + k_y^2}$ where $\mathbf{k} = (k_x, k_y) \in (-\pi, \pi]^2$.
- Frequency band of the object wave: $\mathcal{B}_\mathrm{O}$ is assumed to be a disk centered at the frequency zero with radius ρ (see Fig. 2), which can be estimated from the cutoff frequency of the microscope objective [3, 23, 47]. The larger the value of ρ, the higher the resolution achieved.
- Frequency band of the reference wave: $\mathcal{B}_\mathrm{R}$ is assumed to be small (see Fig. 2) and typically reduces here to a 3×3 block of DFT coefficients after discretization (N_1, N_2 = number of lines/columns of the digital image):

$$A_\mathrm{R}(x,y) = \frac{1}{N_1 N_2} \sum_{\substack{u_1=-1,0,1\\u_2=-1,0,1}} \hat{A}_\mathrm{R}(u_1,u_2)\mathrm{e}^{2i\pi\left(\frac{u_1 x}{N_1}+\frac{u_2 y}{N_2}\right)}$$

- Numerical overlap (NO): a quantification of the overlap between the zeroth order and the twin Fourier bands of an interferogram (visualization in Fig. 4)

$$\mathrm{NO} = \frac{1}{2}\left(\frac{3\rho}{d} - 1\right) = \begin{cases} < 0, & \text{no overlap} \\ \in [0,1), & \text{partial overlap} \\ \geq 1, & \text{full overlap} \end{cases} \quad \textbf{(6)}$$

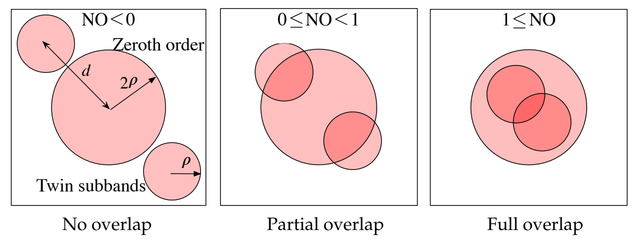

Fig. 4. Visual depiction of the main bandwidth parameters, and their combination into a "Numerical Overlap" (NO).

Assuming that the interferogram is spatially sampled at a frequency large enough so that the object and twin frequency bands are not aliased, means that $\rho + \max(|k_x|, |k_y|) \leq \pi$. Then, given that the interferogram is made of *real*-valued numbers whereas the object wave is made of *complex*-valued numbers, we cannot expect to reconstruct unambiguously the object wave if the surface of its bandwidth, $\pi\rho^2$, is larger than half the surface of the Nyquist rectangle, $(2\pi)^2$: this implies that ρ should be smaller than $\sqrt{2\pi}$.

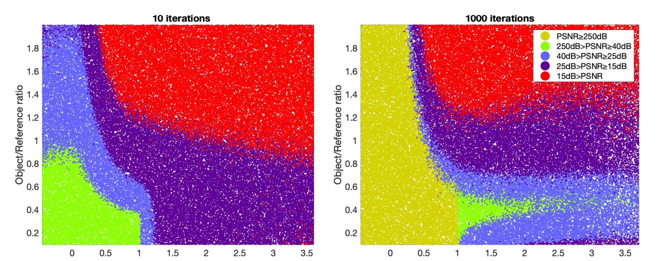

Fig. 5. Reconstruction accuracy of the algorithm (left, 10 iterations, right 1000 iterations) for 100,000 random realizations of the complex wave image, and of the parameters ρ (object bandwidth), $\mathbf{k}$ (reference frequency), NO (Numerical Overlap), and O/R (Object/Reference amplitude ratio): NO and O/R alone are sufficient to predict the accuracy of our algorithm.

An extensive simulation (100,000 random tests) involving all possible O/R values in $[0.1, 2]$, $\rho \leq \sqrt{2\pi}$, $\mathbf{k} = (k_x, k_y) \in [-\pi, \pi]^2$ and NO $\in [-0.5, 3.7]$ on i.i.d. white noise images (filtered in the bandwidth $\mathcal{B}_\mathrm{O}$) shows that the reconstruction PSNR is essentially predicted by a combination of NO and O/R; i.e., accuracy is not dependent on the actual size of the bandwidth of the object wave.

This simulation also suggests that our algorithm converges to the exact solution (PSNR ≥ 250 dB) for a wide range of choices

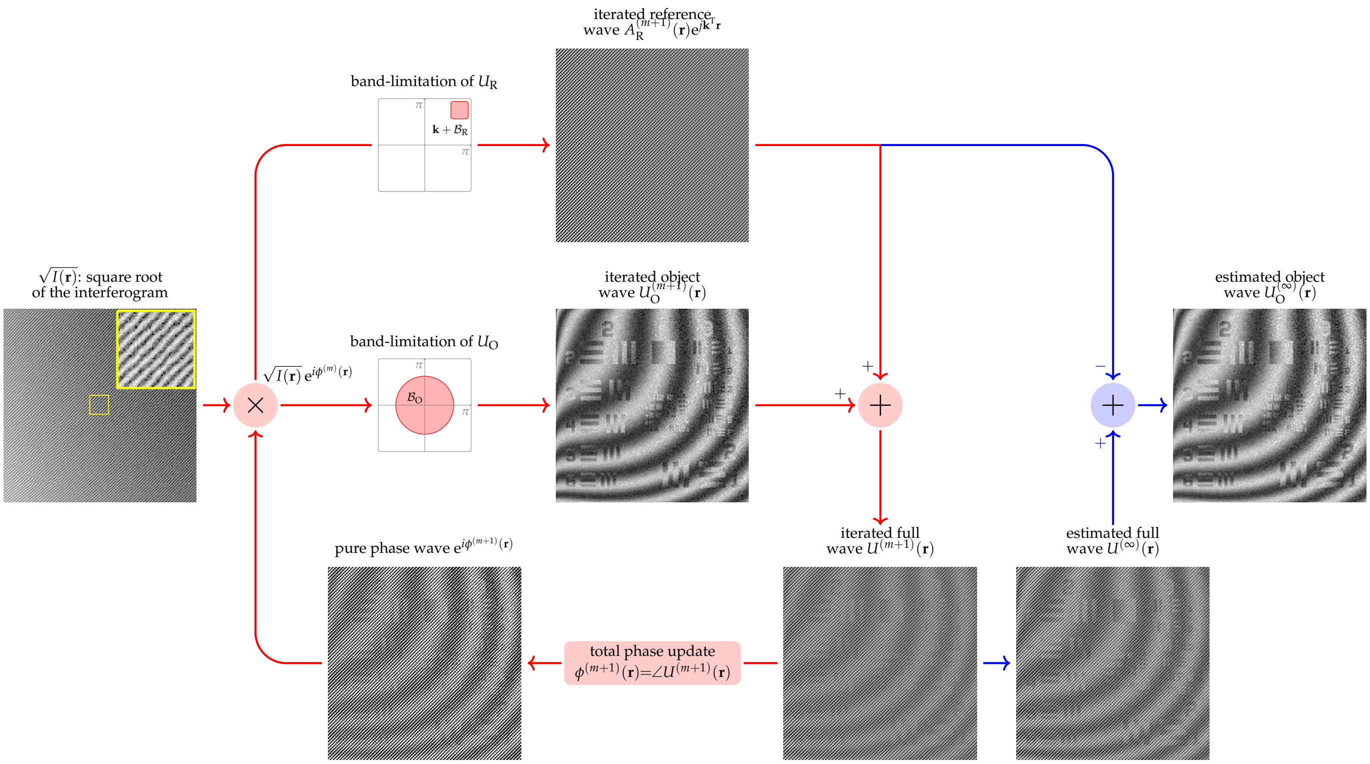

Fig. 6. Flow chart of the complex wave retrieval algorithm (red/blue: iterated/non-iterated parts).

of NO and O/R, in particular when NO ≤ 1 together with O/R ≤ 0.6. For most practical values of interest, moreover, the PSNR results obtained are compatible with a reasonably accurate reconstruction (i.e., PSNR ≥ 25 dB), and this with as few as 10 iterations. Note also that the theoretically maximum resolution $\rho \approx \sqrt{2\pi}$ can be achieved with good accuracy when, e.g., the object/reference ratio is between 0.2 and 0.7.

B. Phase Restoration Algorithm

After complex wave retrieval, unwanted distorted phase (usually $> 2\pi$) inevitably appears and degrades the contrast. It originates partially from the intrinsic phase distortion of the reference wave, from an inaccurate estimation of the reference frequency, but also from a mismatch between refractive indices of coverslips, surrounding medium, etc. Non-linear polynomial phase distortion, in particular, is more common in practical high transverse magnification optical system [41].

Conventionally, phase distortion is compensated in two steps: phase unwrapping, followed by another processing like polynomial fitting [11, 52], PCA [53, 54], or CNN-[55]. The most standard consists in performing least-squares polynomial fitting (Zernike or Chebyshev bases) [42, 43] over a large object-free zone that is identified manually. As mentioned earlier, errors are likely to be introduced in the phase unwrapping process because of noise, or phase discontinuity. To mitigate this issue, we are proposing here a method to estimate the phase distortion in one step; i.e., without resorting to phase unwrapping. As a bonus, we do not need to specify the object-free fitting region.

In a nutshell, our method consists in identifying iteratively a "reliable" subset of the phase map (typically, of 8-connected values [56] that are sufficiently close to each other, making it likely that they are within the same wrapping interval), then fitting only these phase values with a spatial polynomial [43], then extrapolating the phase distortion outside the fitting range—thereby avoiding the unwrapping process. The polynomial phase map obtained is finally subtracted to the wrapped phase map (modulo 2π). How close should the (absolute) phase differences within the connected region be? Less than π, so as to ensure that adding or removing 2π to a phase value always results in a larger phase difference. Here, we choose phase values in $(-\pi/2, \pi/2)$.

Not only is this approach very robust to noise and other inaccuracies, but it is also computationally quite simple, despite being iterative. More specifically, a 2D Chebyshev polynomial estimate $\phi_d^{(m)}(\mathbf{r})$ of the distortion of the phase of $U_O(\mathbf{r})$ at iteration m is obtained by iterating the following steps (see Fig. 7):

- Find the largest 8-connected set of points, $\mathcal{C}$ (Matlab function `bwareafilt`), for which the values of $\phi(\mathbf{r}) = \arg\{U_O(\mathbf{r})e^{-j\phi_d^{(m)}(\mathbf{r})}\}$ are inside the interval $(-\pi/2, \pi/2)$;
- Least-square fit the values of $\phi(\mathbf{r})$ only for $\mathbf{r} \in \mathcal{C}$, with a spatial polynomial expressed on a 2D Chebyshev polynomial basis $\rightarrow \delta\phi_d^{(m)}(\mathbf{r})$;
- Update $\phi_d^{(m+1)}(\mathbf{r}) = \phi_d^{(m)}(\mathbf{r}) + \delta\phi_d^{(m)}(\mathbf{r})$.

The initial distortion estimate is $\phi_d^{(0)}(\mathbf{r}) = 0$. We stop the iterations when the maximal value of $|\delta\phi^{(m)}(\mathbf{r})|$ is smaller than 10^{-2} which typically happens in just a few iterations.

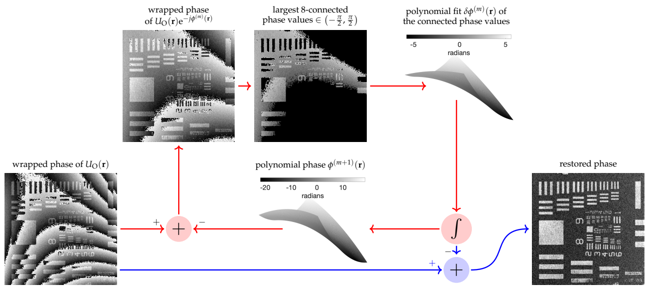

Fig. 7. Flow chart of the phase restoration algorithm (red/blue: iterated/non-iterated parts). The "$\int$" block denotes a summation over all previous iterates. See supplement 1 for a pdf-animated visualization.

3. NUMERICAL EXPERIMENTS

For the sake of simplicity, we test the two algorithms presented in this paper separately. First, we demonstrate the superior quality achieved by our complex wave retrieval algorithm (CWR) in a comprehensive PSNR comparative study for a large range of the parameters O/R, NO, and ρ, in function of the PSNR of the noise added to the interferogram. Then, we demonstrate the efficiency of our phase restoration algorithm (low computation cost, high quality, simplicity) on a specific example. All the experiments performed in this paper are carried out using MATLAB R2018b (MathWorks Inc., Natick, Massachusetts, USA) on a desktop computer (Intel Core i7-7700K CPU, 4.2 GHz, 32 GB RAM). The code will be made available at the time of publication.

A. Complex Wave Reconstruction

Additive white Gaussian noise (AWGN) is added to the interferogram that encodes an object wave made of a synthetic "Spoke" phase image (512× 512 pixels, large phase range: $[-0.2, 2.7]$ radian). For comparison purposes, Baek's algorithm [23] [1], the standard FT approach and a recent total variation-based compressive sensing (CS) method [24] are chosen. However, in order to retrieve the object wave, it is necessary to estimate the reference wave, which is done in Baek's algorithm by a second measurement, whereas the other two methods choose to ignore this issue. We thus re-normalize (least-square fit of a complex-valued factor with the ground-truth) the results of all the algorithms to make it possible to evaluate their reconstruction PSNR.

We use Baek's code according to the author's suggestions to obtain the best results. We have implemented the CS algorithm following the author's suggestion in a private email (i.e., use the FISTA code provided by A. Beck [2], to ensure an equivalently efficient implementation), and set the parameters according to his paper, with the exception of the regularization parameter which we optimize for each image (visual quality).

The experimental reconstruction results from more than 3000 tests, varying the numerical overlap NO, the object bandwidth ρ, and the noise PSNR are visualized in Fig. 8. We do not compare with the CS method here because it is too slow and moreover, requires manual tuning for ideal results. When the frequency bands of the zeroth order and the twin images are well-separated (NO ≤ 0), all CWR methods achieve acceptable accuracy (PSNR$>$ 20 dB, depending on the input noise level) as can be seen in Fig. 8 (*left*), with the FT leading the pack when the noise PSNR is larger than 30 dB. When NO>0, however, our complex wave retrieval algorithm exhibits the highest reconstruction accuracy, irrespective of the noise level. The reconstruction accuracy of FT decreases rapidly to about 5 dB, in fact. If we focus on the object bandwidth and fix NO $= 0.7$, instead, our algorithm outperforms the others significantly (median PSNR difference between our method and Baek's is about 1.8 dB) as evidenced by Fig. 8 (*right*).

The real part of a typical result is shown in Fig. 9 (CS regularization parameter set to 10 as suggested in [24]). Our CWR algorithm achieves significantly better reconstruction quality than other methods. In particular, Gibbs and fringe-like artifacts can be identified in Baek's algorithm—likely as a consequence of zero-padding and unsuccessful suppression of the zeroth order. The poor quality of the Fourier method is due to the large overlap between the twin images and the zeroth order. The CS method seems to achieve a better resolution than Baek's (probably due to the piecewise-constant nature of the images), but at the expense of a significantly higher computational cost.

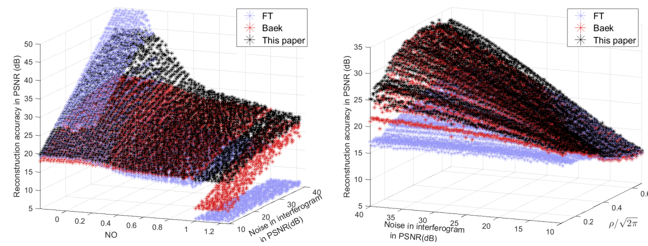

Fig. 8. Better overall performance of our complex wave retrieval algorithm (10 iterations), compared to the standard Fourier approach (FT) and Baek's algorithm [23], under various noise levels. Left: the numerical overlap varies in $[-0.5, 1.5]$, but the object bandwidth ρ is set to $\sqrt{2\pi}/5$; right: ρ varies in $[\sqrt{2\pi}/10, \sqrt{2\pi}/1.5]$, but numerical overlap (NO) is set to 0.7 (amplitude ratio O/R $= 0.7$).

B. Phase Restoration

In general, it is phase discontinuities and noise that make phase restoration challenging. To evaluate our algorithm in such conditions, we have chosen a USAF phase target (512×512 pixels) with a large range of values ($\in [-0.31, 2.54]$ radians) and sharp edges. For comparison purposes, the standard unwrap-and-fit phase restoration strategy is evaluated with two open source phase unwrapping algorithms PUMA[3] (Phase Unwrapping MAx-flow) [58], and TIE[4] (Transport of Intensity Equation) [57].

Our observation is that, when the USAF phase image is distorted by a 2D polynomial of degree 4, further corrupted by additive white Gaussian noise of various intensities, our algorithm and the unwrap-and-fit methods have a similar performance, but that ours is significantly faster: the computation bottleneck is, of course, the unwrapping algorithm, which our method does not use. However, when the "noise" is not random and contains high frequencies (from, e.g., the concentric fringes that arise from isolated point scatterers, like impurities or dust particles), a significant difference in quality appears, as shown in Fig. 10. Also note that our method does not need to identify an object-free region to calculate the quadratic distortion, contrary to the unwrap-and-fit approaches.

[1] code released by the author: https://opticapublishing.figshare.com/articles/journal_contribution/3712889_pdf/7423859
[2] https://sites.google.com/site/amirbeck314/software
[3] http://www.lx.it.pt/~bioucas/code.htm
[4] https://ww2.mathworks.cn/matlabcentral/fileexchange/68493-robust-2d-phase-unwrapping-algorithm

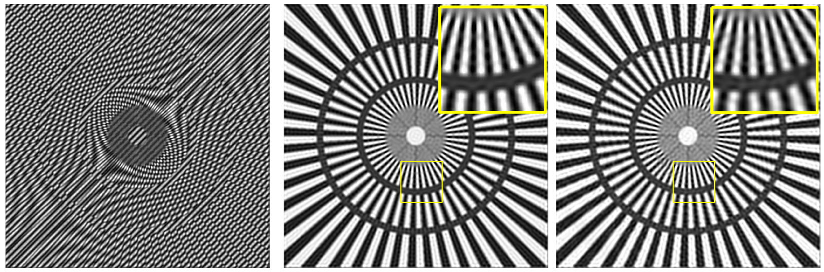

Synthetic interferogram with noise in PSNR: 30 dB | Ground-truth | This paper PSNR: 24.9 dB Time: 0.25s (5 iterations)

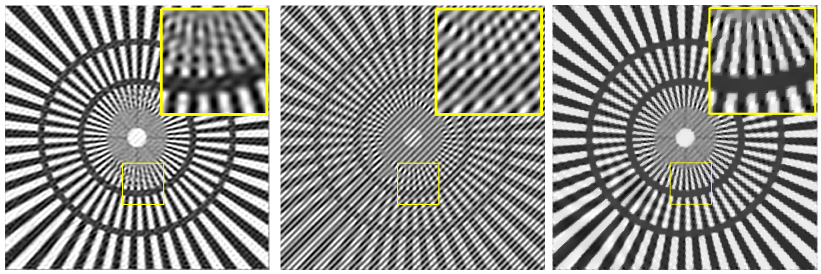

Baek's paper [23] PSNR: 19.3 dB Time: 0.30s | FT method PSNR: 6.8 dB Time: 0.03s | CS method [24] PSNR: 18.3 dB Time: 165s

Fig. 9. Higher quality of our Complex Wave Retrieval algorithm in simulated noisy conditions (O/R $= 0.7$, NO $= 1.3$, $\rho = \sqrt{2\pi}/3$, $k_x = k_y$). To ensure fairness of the comparison, the reconstructed images (real-part only) are shown with the same intensity scale.

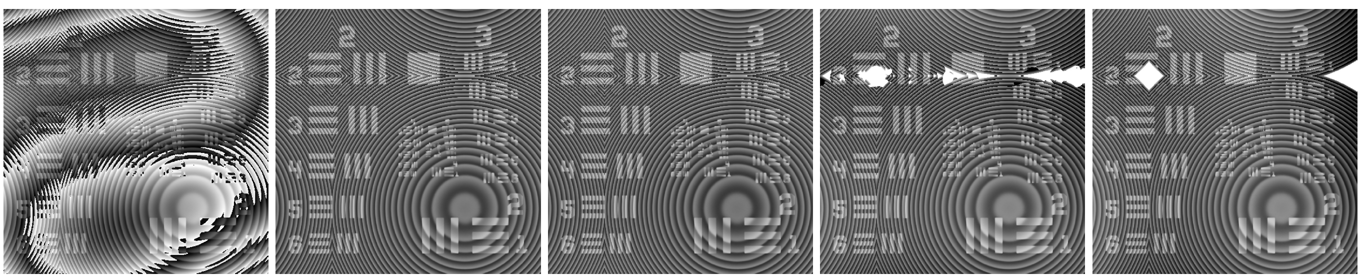

Synthetic wrapped phase | Ground-truth phase | This paper PSNR: 31.0 dB Time: 0.25s (5 iterations) | Unwrap [57] PSNR: 9.2 dB Time: 6.9s | Unwrap [58] PSNR: 8.6 dB Time: 6.5s

Fig. 10. Direct polynomial fitting (central image) of the raw "wrapped" phase is not only much faster than an unwrap-and-fit strategy (the two rightmost images), but can also be significantly more accurate for images that have non-random high frequencies like the phase image in the leftmost column. Here, a polynomial of degree 4 is used to fit the distortion.

4. REAL EXPERIMENTS

We first consider the interferograms of the "USAF" and "Spoke" phase targets. The height of the patterns seen in these targets is known to be 350 nm, which allows us to compare image reconstruction methods visually and quantitatively. We then consider the interferogram of a tobacco BY-2 plant cell. Note that, in order to be able to compare the performance of our algorithm with Baek's method, we also had to acquire a reference wave intensity image of each imaged sample: these extra interferograms were not used by our algorithm, though.

A. Complex Wave Retrieval

In order to ensure that the object wave is frequency limited within a band of radius $\pi/2$, the interferometric system depicted in Fig. 1(a) was designed with the following parameters [23, 47]: laser of wavelength $\lambda = 0.532\,\mu$m, microscope objective NA $=$ 0.8, camera pixel size $=$ 3.45 μm, and system magnification ≈ 21.2. In order to test the reconstruction under full overlap of the interferogram, the reference wave frequency was changed by altering the tilt angle between the reference wave and the object wave. This was done with the help a real-time GUI which monitors the frequency spectrum of the interferogram.

Figure 11 shows the phase reconstructed from the 2048×2048 USAF interferogram (FOV $= 0.33 \times 0.33\,\text{mm}^2$) under full overlap (NO = 1.7). For the CS method [24], the regularization parameter is tuned to 10^{-4} in Figs. 11 and 13. Here, the reference wave exhibits a slowly varying amplitude, which we account for by assuming that its discrete spatial frequency band, $\mathcal{B}_{\mathrm{R}}$ (see Section A), is a 3×3 square—9 complex-valued Fourier coefficients. After CWR, the phase is unwrapped (PUMA algorithm [58]) and then, a 2D polynomial fit of degree 4 is performed to undo the global distortion of the phase image. Note that we do not use our phase restoration algorithm here, because we want to compare only the quality of the complex wave retrieval between different algorithms. However, see supplement 1 for the results with our own (much faster: below 15 seconds) phase restoration algorithm.

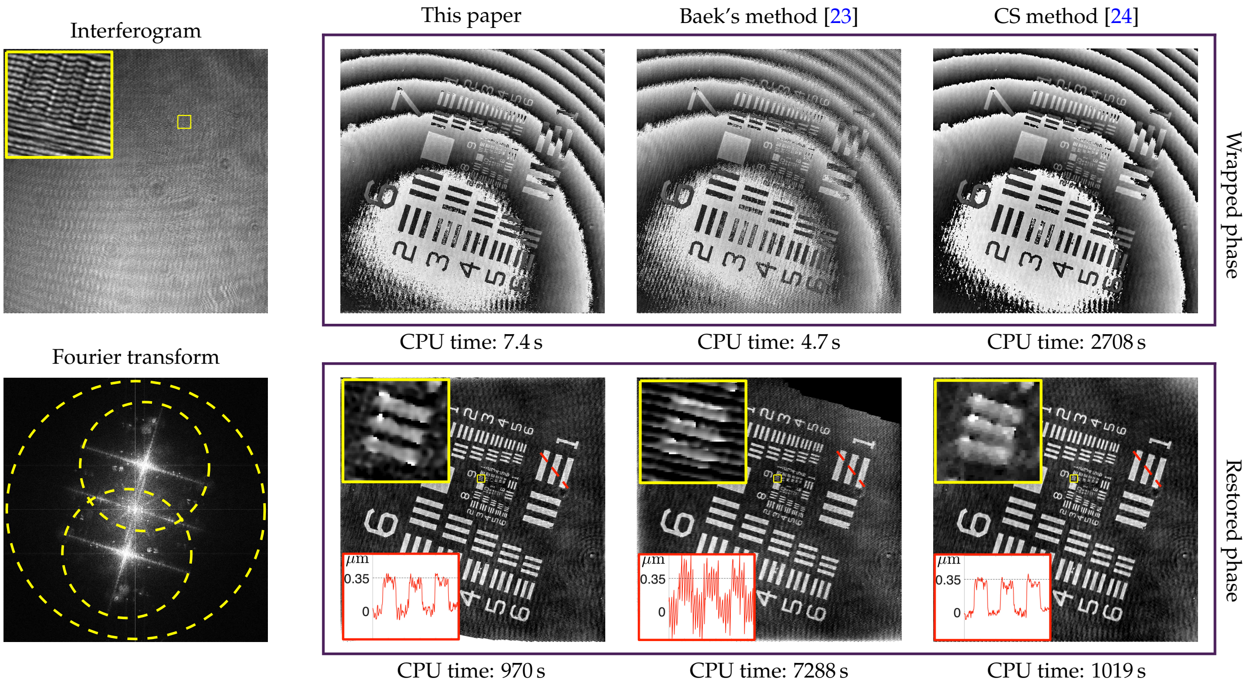

Fig. 11. Wrapped phase (top row) obtained via different complex wave retrieval methods, and restored phase (bottom row) using PUMA unwrap [58] + degree-4 polynomial fit. Note the fringe-like artifacts in Baek's results, and their absence in the other two methods: these high-frequency artifacts are the likely cause of a significantly longer phase unwrapping time. The standard deviation of the phase in object-free areas (excluding obvious outliers) is about 0.24 radians ($\approx$ 39 nm height value) for our algorithm, 0.35 radians ($\approx$ 57 nm height value) for Baek's algorithm and 0.20 radians ($\approx$ 33 nm height value) for the CS method. Scale bar indicates 20 μm.

As shown in Fig. 11, our algorithm achieves the best resolution compared to the other methods (zoom). On the other hand, CS exhibits a slightly smaller phase fluctuation. Particularly noticeable in Baek's result are strong fringe artifacts that are already present in the wrapped phase, then in the restored phase; also note the large fluctuations of the height (about 57 nm, calculated by Eq. (1a) defined in Ref. [10]) along the red line. A calculation of the standard deviation of the phase in empty zones (excluding unwrap-related saturation errors) shows that these fluctuations are significantly larger in Baek's result (0.35 radians versus 0.24 radians in ours, and 0.20 radians in CS).These artifacts (their high-frequency) are likely the reason why the unwrapping algorithm used for phase restoration require so much more computation time for Baek's wrapped phase. Note again the very high computational cost of the CS method, which makes optimal tuning of the regularization parameter almost unfeasible in practice (required more than one day in this example).

B. Phase Restoration

We validate our restoration algorithm using a physical "spoke" phase target with a pattern height of 350 nm, and compare with unwrap-and-fit algorithms that use the PUMA [58] and TIE [57] unwrapping algorithms. In details, an interferogram of the "spoke" target is acquired (2048 $\times$ 2048 pixels, NO $= 1.3$, O/R $= 0.7$ and $\rho = \pi/2$) and the complex object wave is retrieved using our CWR algorithm. As previously, 9 Fourier coefficients are used to parameterize the amplitude of the reference wave. It is the (wrapped) phase of the complex image obtained that is input to the phase restoration algorithms. Empirically, a 2D polynomial of degree no less than 5 is able to approximate reasonably well the phase distortion observed.

As can be seen in Fig. 12, our restoration provides a phase image that is visually on par with that from the PUMA unwrap-and-fit method, but also is significantly better than that from the TIE unwrap-and-fit method, especially in the image center where the phase varies fast. The height values along the red dashed line (low frequency variations) for all approaches match well the ground-truth height (350 nm). Even more significantly, our phase restoration algorithm requires but a small fraction of the computation time of the two other algorithms.

C. Complex Imaging of Biological Cells

Finally, we show that we can image biological cells by applying our complex wave retrieval and phase restoration. In details, we acquire the interferogram of tobacco BY-2 cells using a camera with larger pixel size (4.8 μm) than the previous experiments, in such a way as to ensure that the object wave has a large bandwidth: $\rho \approx 2.1$, according to cutoff frequency formula Eq. (13) in Ref. [47]. This and the angle between the object with reference waves also lead to a large numerical overlap: NO $= 1.73$.

As previously, our complex wave retrieval algorithm uses 9 Fourier coefficients to parameterize the variations of amplitude of the reference wave. We also observe that a 2D polynomial of degree 3 is sufficient to approximate well the global phase distortion of the complex object wave. We show in Fig. 13 the phase reconstruction obtained using different algorithms. It should be noted that, because the final phase variation of the object is larger than 2π, a further unwrapping may be needed after our restoration. However, we also show the result (bottom-left image in Fig. 13) without this last step to demonstrate the already high quality of the result obtained and a near perfect correction of the global phase distortion.

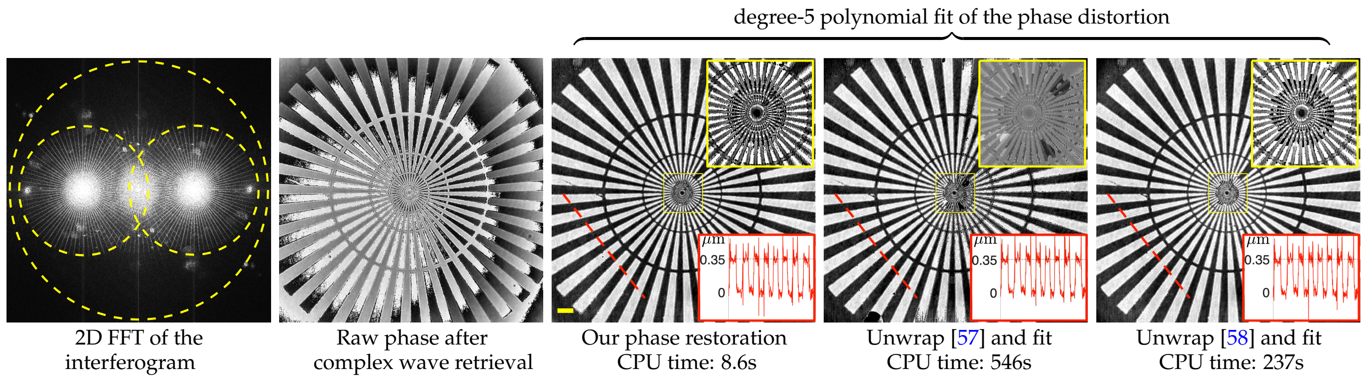

Fig. 12. Phase restoration from the complex wave retrieved (using the algorithm of Section A) from a real interferogram (2048 × 2048 pixels, NO = 1.3, O/R = 0.7 and $\rho = \pi/2$). In addition to visual quality, note the significantly lower computation time required by our method, compared to the standard unwrap-and-fit algorithms. The standard deviation of the phase in object-free areas (excluding obvious outliers) is about 0.2 radians (≈32 nm height value) for the three methods. Scale bar indicates 20 μm.

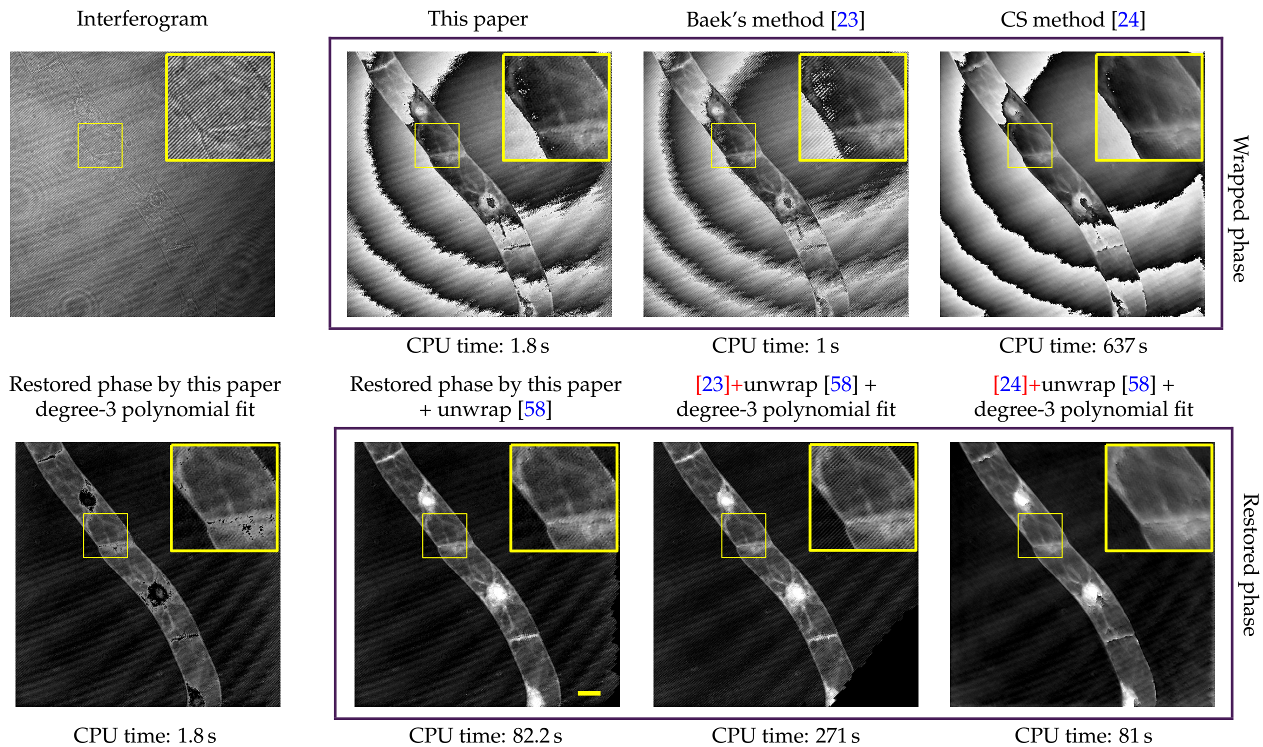

Fig. 13. Comparison of phase retrieval from an interferogram (1024×1024 pixels) of tobacco BY-2 cells with high bandwidth ($\rho \approx 2.1$) and large numerical overlap (NO = 1.73). The standard deviation of the phase in the object-free region is 0.24 radians (≈ 20 nm) in our method, 0.39 radians (≈ 33 nm) in Baek's results, and 0.19 radians (≈ 16 nm) in the CS method. Our results exhibit noticeably fewer fringe-like artifacts than Baek's result, and a higher resolution than that the CS method. Note that phase unwrapping is still needed after our phase restoration (bottom, left) because the cell-induced phase variations are beyond 2π. Scale bar indicates 20 μm.

The obvious fringe-like artifacts present in Baek's wrapped phase result carry over to the unwrapped result, in contrast with the cleaner image produced by our algorithm and the CS method. This phase inaccuracy is also observed in object-free regions where the standard deviation in Baek's result (0.39 radians) is significantly larger than in ours (0.24 radians) and CS (0.19 radians), arguably making small cellular structures more difficult to observe. Again, notice the resolution loss of the CS method, likely traded for a better visual quality.

5. CONCLUSION

In this paper, we have developed a single-frame complex wave retrieval algorithm and an algorithm to remove a global (polynomial) phase distortion, without resorting to phase unwrapping. We have demonstrated extensively by numerical simulations and experiments that our CWR provides accurate, robust results in a wide range of scenarios: large object bandwidth, overlap between twin frequency bands, amplitude ratio between object and reference waves. We have in particular proposed a quantitative measure of this overlap, the "Numerical Overlap" (NO).

The main advantages of our complex wave retrieval algorithm are:

1. Single-frame acquisition, no need for extra acquisition of object-free interferogram or reference wave intensity in contrast with the current state-of-the-art [20–24]. This is particularly useful to enable a higher throughput of quantitative

phase imaging.

2. NO $\gtrsim 1$: Significant overlap between the frequency bands of the twin images and the zeroth order, but also between the twin images themselves. This makes it possible to a more flexible multiplexing design, and process interferograms acquired with very diverse incidence illuminations, enabling implementation in Optical Diffraction Tomography.
3. $\rho \gtrsim \pi/2$: Significant increase of the allowed object bandwidth from, e.g., $\rho = \pi/2$ (see [23]) up to (ideally) $\sqrt{2\pi}$; i.e., more than 150% increase, although we have tested experimentally only an improvement of about 80% (see Section C).
4. O/R ~ 1: Large range of amplitude ratios between the object and the reference wave (even larger than 1, see supplement 1 for details). A ratio close to 1 is known to maximize the SNR and fringe contrast [50, 51], hence increases the accuracy of the recovered complex wave. Having the object more clearly visible in the interferogram also avoids ill-positioned or defocused image acquisitions.
5. Efficient numerical implementation (use of FFT's only) making the algorithm reasonably fast already, and promising even faster performance, due to the availability of specialized FFT circuits.

Removing phase distortions like astigmatism, coma, and spherical aberration is necessary when dealing with interferograms. The main advantages of our phase restoration algorithm is that it does not require any prior unwrapping step, making it significantly faster than approaches based on unwrapping, with no loss of quality. Moreover, due to the occasional failure of unwrapping algorithms when deterministic high-frequency noise is present, the quality of our phase restoration algorithm may be significantly higher than those approaches. Note, however, that in the case of objects that exhibit larger phase variations than 2π, a further unwrapping step (albeit, reduced to the object) may be necessary after phase restoration.

Funding. This work was supported by a grant AoE/M-05/12 from the Hong Kong Research Grants Council, The Chinese University of Hong Kong Research Sustainability of Major RGC Funding Schemes – Strategic Areas and Hong Kong Innovation and Technology Fund grant ITS/148/20.

Acknowledgments. We thank Dr. Yonglun Zeng for the providing the tobacco BY-2 plant cell sample.

Disclosures. The authors declare no conflicts of interest.

Data availability. Data underlying the results presented in this paper are not publicly available at this time but may be obtained from the authors upon reasonable request.

Supplemental document. See Supplement 1 for supporting content.

REFERENCES

1. D. Gabor, "A new microscopic principle," Nature **161**, 777–778 (1948).
2. F. Zernike, "Phase contrast, a new method for the microscopic observation of transparent objects," Physica **9**, 686–698 (1942).
3. J. W. Goodman and R. Lawrence, "Digital image formation from electronically detected holograms," Appl. Phys. Lett. **11**, 77–79 (1967).
4. K. J. Gåsvik, *Optical metrology* (John Wiley & Sons, 2003).
5. G. Zheng, R. Horstmeyer, and C. Yang, "Wide-field, high-resolution Fourier ptychographic microscopy," Nat. Photonics **7**, 739–745 (2013).
6. Y. Park, C. Depeursinge, and G. Popescu, "Quantitative phase imaging in biomedicine," Nat. Photonics **12**, 578–589 (2018).
7. B. Bhaduri, C. Edwards, H. Pham, R. Zhou, T. H. Nguyen, L. L. Goddard, and G. Popescu, "Diffraction phase microscopy: principles and applications in materials and life sciences," Adv. Opt. Photonics **6**, 57–119 (2014).
8. T. Kim, R. Zhou, M. Mir, S. D. Babacan, P. S. Carney, L. L. Goddard, and G. Popescu, "White-light diffraction tomography of unlabelled live cells," Nat. Photonics **8**, 256–263 (2014).
9. H. V. Pham, C. Edwards, L. L. Goddard, and G. Popescu, "Fast phase reconstruction in white light diffraction phase microscopy," Appl. Opt. **52**, A97–A101 (2013).
10. M. Niu, G. Luo, X. Shu, F. Qu, S. Zhou, Y.-P. Ho, N. Zhao, and R. Zhou, "Portable quantitative phase microscope for material metrology and biological imaging," Photonics Res. **8**, 1253–1259 (2020).
11. L. Miccio, D. Alfieri, S. Grilli, P. Ferraro, A. Finizio, L. De Petrocellis, and S. Nicola, "Direct full compensation of the aberrations in quantitative phase microscopy of thin objects by a single digital hologram," Appl. Phys. Lett. **90**, 041104 (2007).
12. M. Trusiak, "Fringe analysis: single-shot or two-frames? Quantitative phase imaging answers," Opt. Express **29**, 18192–18211 (2021).
13. G. Dardikman and N. T. Shaked, "Is multiplexed off-axis holography for quantitative phase imaging more spatial bandwidth-efficient than on-axis holography?" JOSA A **36**, A1–A11 (2019).
14. M. Takeda, H. Ina, and S. Kobayashi, "Fourier-transform method of fringe-pattern analysis for computer-based topography and interferometry," JOSA **72**, 156–160 (1982).
15. E. Sánchez-Ortiga, A. Doblas, G. Saavedra, M. Martínez-Corral, and J. Garcia-Sucerquia, "Off-axis digital holographic microscopy: practical design parameters for operating at diffraction limit," Appl. Opt. **53**, 2058–2066 (2014).
16. I. Yamaguchi and T. Zhang, "Phase-shifting digital holography," Opt. Lett. **22**, 1268–1270 (1997).
17. J.-P. Liu, T.-C. Poon, G.-S. Jhou, and P.-J. Chen, "Comparison of two-, three-, and four-exposure quadrature phase-shifting holography," Appl. Opt. **50**, 2443–2450 (2011).
18. N. T. Shaked, V. Micó, M. Trusiak, A. Kuś, and S. K. Mirsky, "Off-axis digital holographic multiplexing for rapid wavefront acquisition and processing," Adv. Opt. Photonics **12**, 556–611 (2020).
19. M. Liebling, T. Blu, and M. Unser, "Complex-wave retrieval from a single off-axis hologram," JOSA A **21**, 367–377 (2004).
20. C. S. Seelamantula, N. Pavillon, C. Depeursinge, and M. Unser, "Exact complex-wave reconstruction in digital holography," JOSA A **28**, 983–992 (2011).
21. C. S. Seelamantula, B. A. Shenoy, S. Coquoz, and T. Lasser, "Exact reconstruction in Quantitative Phase Microscopy," in *2014 IEEE International Conference on Image Processing (ICIP),* (IEEE, 2014), pp. 3934–3938.
22. D. Kim, R. Magnusson, M. Jin, J. Lee, and W. Chegal, "Complex object wave direct extraction method in off-axis digital holography," Opt. Express **21**, 3658–3668 (2013).
23. Y. Baek, K. Lee, S. Shin, and Y. Park, "Kramers–Kronig holographic imaging for high-space-bandwidth product," Optica **6**, 45–51 (2019).
24. S. Yoshida, "Compressed off-axis digital holography," J. Opt. **22**, 095703 (2020).
25. W. Zhang, L. Cao, D. J. Brady, H. Zhang, J. Cang, H. Zhang, and G. Jin, "Twin-image-free holography: a compressive sensing approach," Phys. Rev. Lett. **121**, 093902 (2018).
26. L. Denis, D. Lorenz, E. Thiébaut, C. Fournier, and D. Trede, "Inline hologram reconstruction with sparsity constraints," Opt. Lett. **34**, 3475–3477 (2009).
27. V. Katkovnik, I. Shevkunov, N. Petrov, and K. Egiazarian, "Wavefront reconstruction in digital off-axis holography via sparse coding of amplitude and absolute phase," Opt. Lett. **40**, 2417–2420 (2015).
28. B. L. Reddy, P. Ramachandran, and A. Nelleri, "Compressive complex wave retrieval from a single off-axis digital Fresnel hologram for quantitative phase imaging and microlens characterization," Opt. Commun. **478**, 126371 (2021).
29. K. G. Larkin, D. J. Bone, and M. A. Oldfield, "Natural demodulation of two-dimensional fringe patterns. I. General background of the spiral

phase quadrature transform," JOSA A **18**, 1862–1870 (2001).
30. K. G. Larkin, "Natural demodulation of two-dimensional fringe patterns. II. Stationary phase analysis of the spiral phase quadrature transform," JOSA A **18**, 1871–1881 (2001).
31. C. S. Seelamantula, N. Pavillon, C. Depeursinge, and M. Unser, "Local demodulation of holograms using the Riesz transform with application to microscopy," JOSA A **29**, 2118–2129 (2012).
32. M. Kaseb, G. Mercère, H. Biermé, F. Brémand, and P. Carré, "Phase estimation of a 2D fringe pattern using a monogenic-based multiscale analysis," JOSA A **36**, C143–C153 (2019).
33. Y. Tounsi, M. Kumar, A. Siari, F. Mendoza-Santoyo, A. Nassim, and O. Matoba, "Digital four-step phase-shifting technique from a single fringe pattern using Riesz transform," Opt. Lett. **44**, 3434–3437 (2019).
34. J. R. Fienup, "Reconstruction of an object from the modulus of its Fourier transform," Opt. Lett. **3**, 27–29 (1978).
35. R. W. Gerchberg, "A practical algorithm for the determination of phase from image and diffraction plane pictures," Optik **35**, 237–246 (1972).
36. Y. Shechtman, Y. C. Eldar, O. Cohen, H. N. Chapman, J. Miao, and M. Segev, "Phase retrieval with application to optical imaging: a contemporary overview," IEEE Signal Process. Mag. **32**, 87–109 (2015).
37. E. J. R. Pauwels, A. Beck, Y. C. Eldar, and S. Sabach, "On Fienup methods for sparse phase retrieval," IEEE Trans. on Signal Process. **66**, 982–991 (2017).
38. A. Sinha, J. Lee, S. Li, and G. Barbastathis, "Lensless computational imaging through deep learning," Optica **4**, 1117–1125 (2017).
39. Y. Rivenson, Y. Zhang, H. Günaydın, D. Teng, and A. Ozcan, "Phase recovery and holographic image reconstruction using deep learning in neural networks," Light. Sci. & Appl. **7**, 17141–17141 (2018).
40. X. Shu, Y. Zhang, M. Niu, W. Luo, and R. Zhou, "Compact and ease-of-use quantitative phase microscopy for real-time live-cell imaging," in *Quantitative Phase Imaging VIII,* vol. 11970 (SPIE, 2022), pp. 13–18.
41. R. W. Meier, "Magnification and third-order aberrations in holography," JOSA **55**, 987–992 (1965).
42. J. C. Wyant and K. Creath, "Basic wavefront aberration theory for optical metrology," Appl. Opt. Opt. Eng. **11**, 28–39 (1992).
43. J. Ye, Z. Gao, S. Wang, J. Cheng, W. Wang, and W. Sun, "Comparative assessment of orthogonal polynomials for wavefront reconstruction over the square aperture," JOSA A **31**, 2304–2311 (2014).
44. D. Blinder, H. Ottevaere, A. Munteanu, and P. Schelkens, "Efficient multiscale phase unwrapping methodology with modulo wavelet transform," Opt. Express **24**, 23094–23108 (2016).
45. U. S. Kamilov, I. N. Papadopoulos, M. H. Shoreh, D. Psaltis, and M. Unser, "Isotropic inverse-problem approach for two-dimensional phase unwrapping," JOSA A **32**, 1092–1100 (2015).
46. Z. Ren, J. Zhao, and E. Y. Lam, "Automatic compensation of phase aberrations in digital holographic microscopy based on sparse optimization," APL Photonics **4**, 110808 (2019).
47. N. Pavillon, C. S. Seelamantula, J. Kühn, M. Unser, and C. Depeursinge, "Suppression of the zero-order term in off-axis digital holography through nonlinear filtering," Appl. Opt. **48**, H186–H195 (2009).
48. K. Lange, *MM optimization algorithms* (SIAM, 2016).
49. N. Fu, P. Zheng, X. Li, and L. Qiao, "Weighted phase retrieval of Fourier measurement with outliers: measurement structure and reconstruction algorithm," IEEE Trans. on Instrum. Meas. **70**, 1–14 (2020).
50. P. Picart and J.-c. Li, *Digital holography* (John Wiley & Sons, 2013).
51. P. A. Cheremkhin, N. N. Evtikhiev, V. V. Krasnov, V. G. Rodin, and R. S. Starikov, "Shot noise and fixed-pattern noise effects on digital hologram reconstruction," Opt. Lasers Eng. **139**, 106461 (2021).
52. T. Colomb, E. Cuche, F. Charrière, J. Kühn, N. Aspert, F. Montfort, P. Marquet, and C. Depeursinge, "Automatic procedure for aberration compensation in digital holographic microscopy and applications to specimen shape compensation," Appl. Opt. **45**, 851–863 (2006).
53. C. Zuo, Q. Chen, W. Qu, and A. Asundi, "Phase aberration compensation in digital holographic microscopy based on principal component analysis," Opt. Lett. **38**, 1724–1726 (2013).
54. X. Zhang, J. Sun, Z. Zhang, Y. Fan, Q. Chen, and C. Zuo, "Multi-step phase aberration compensation method based on optimal principal component analysis and subsampling for digital holographic microscopy," Appl. Opt. **58**, 389–397 (2019).
55. T. Nguyen, V. Bui, V. Lam, C. B. Raub, L.-C. Chang, and G. Nehmetallah, "Automatic phase aberration compensation for digital holographic microscopy based on deep learning background detection," Opt. Express **25**, 15043–15057 (2017).
56. J. Serra and P. Soille, *Mathematical morphology and its applications to image processing*, vol. 2 (Springer Science & Business Media, 2012).
57. Z. Zhao, H. Zhang, Z. Xiao, H. Du, Y. Zhuang, C. Fan, and H. Zhao, "Robust 2D phase unwrapping algorithm based on the transport of intensity equation," Meas. Sci. Technol. **30**, 015201 (2018).
58. J. M. Bioucas-Dias and G. Valadao, "Phase Unwrapping via Graph Cuts," IEEE Trans. on Image Process. **16**, 698–709 (2007).